Ripple formation on Si surfaces during plasma etching in Cl2

AUTHOR(S):

Nakazaki, Nobuya; Matsumoto, Haruka; Sonobe, Soma; Hatsuse, Takumi; Tsuda, Hirotaka; Takao, Yoshinori; Eriguchi, Koji; Ono, Kouichi

CITATION:

Nakazaki, Nobuya ...[et al]. Ripple formation on Si surfaces during plasma etching in Cl2. AIP Advances 2018, 8(5): 055027.

ISSUE DATE:

2018-05

URL:

http://hdl.handle.net/2433/231937

AIP ADVANCES **8**, 055027 (2018)

Ripple formation on Si surfaces during plasma etching in Cl_2

Nobuya Nakazaki,[1,a] Haruka Matsumoto,[1,b] Soma Sonobe,[1,c] Takumi Hatsuse,[1,b] Hirotaka Tsuda,[1,d] Yoshinori Takao,[1,e] Koji Eriguchi,[1] and Kouichi Ono[1,2,f]

[1]*Department of Aeronautics and Astronautics, Graduate School of Engineering, Kyoto University, Kyoto-daigaku Katsura, Nishikyo-ku, Kyoto 615-8540, Japan*
[2]*Joining and Welding Research Institute, Osaka University, 11-1 Mihogaoka, Ibaraki, Osaka 567-0047, Japan*

(Received 24 November 2017; accepted 11 May 2018; published online 25 May 2018)

Nanoscale surface roughening and ripple formation in response to ion incidence angle has been investigated during inductively coupled plasma etching of Si in Cl_2, using sheath control plates to achieve the off-normal ion incidence on blank substrate surfaces. The sheath control plate consisted of an array of inclined trenches, being set into place on the rf-biased electrode, where their widths and depths were chosen in such a way that the sheath edge was pushed out of the trenches. The distortion of potential distributions and the consequent deflection of ion trajectories above and in the trenches were then analyzed based on electrostatic particle-in-cell simulations of the plasma sheath, to evaluate the angular distributions of ion fluxes incident on substrates pasted on sidewalls and/or at the bottom of the trenches. Experiments showed well-defined periodic sawtooth-like ripples with their wave vector oriented parallel to the direction of ion incidence at intermediate off-normal angles, while relatively weak corrugations or ripplelike structures with the wave vector perpendicular to it at high off-normal angles. Possible mechanisms for the formation of surface ripples during plasma etching are discussed with the help of Monte Carlo simulations of plasma-surface interactions and feature profile evolution. The results indicate the possibility of providing an alternative to ion beam sputtering for self-organized formation of ordered surface nanostructures. https://doi.org/10.1063/1.5017070

I. INTRODUCTION

Atomic- or nanometer-scale roughness on etched feature surfaces has become an important issue to be resolved in the fabrication of nanoscale microelectronic devices.[1,2] The roughness formed on feature sidewalls and bottom surfaces during plasma etching is nowadays often comparable to the critical dimension of the feature and the thickness of the layer being etched and/or the layer underlying, thus leading to an increased variability in device performance.[3,4] A number of studies have been made of surface roughening during plasma etching,[5–7] including sidewall roughening in

[a]Present address: Sony Semiconductor Solutions Corporation, Device Development Division, Atsugi, Kanagawa 243-0014, Japan.
[b]Present address: Nippon Steel & Sumitomo Metal Corporation, Nagoya Works, Tokai, Aichi 476-8686, Japan.
[c]Present address: Nippon Steel & Sumitomo Metal Corporation, Kimitsu Works, Kisarazu, Chiba 299-1141, Japan.
[d]Present address: Toshiba Corporation Semiconductor & Storage Products Company, Center for Semiconductor Research & Development, Kawasaki, Kanagawa 212-8583, Japan.
[e]Present address: Division of Systems Research, Faculty of Engineering, Yokohama National University, Yokohama, Kanagawa 240-8501, Japan.
[f]Electronic mail: ono.kouichi.63s@st.kyoto-u.ac.jp, ono@kuaero.kyoto-u.ac.jp, and ono@jwri.osaka-u.ac.jp

pattern definition;[8–12] a few studies have also been concerned with spontaneous or maskless formation of organized nanostructures such as nanotextures and nanopillars during plasma etching.[13–15] Several mechanisms have been invoked to interpret the experiments,[5–7] including the noise (or stochastic roughening), geometrical shadowing, surface reemission of neutral reactants, micromasking by etch inhibitors, and ion scattering/channeling.

Longitudinal striations or ripplelike structures (called the line edge/width roughness) are often observed to occur on feature sidewalls during plasma etching,[8–12] which are usually appreciated to arise extrinsically from pattern transfer of the mask edge roughness under geometrical shadowing effects for incoming ions;[10] in practice, however, they would also arise intrinsically (or spontaneously) from plasma-surface interactions themselves, because the ions are incident directly on feature sidewalls at high off-normal angles. Spontaneous or self-organized formation of ordered nanostructures such as dots and ripples in response to ion incidence angle on substrate surfaces has been extensively studied during ion beam sputtering (IBS) since decades.[16–21] In contrast, little work has been concerned with surface roughening and rippling in response to ion incidence angle in plasma environments, except for a few plasma etching studies of Sawin *et al.* using plasma beams[22,23] and Monte Carlo (MC) simulations[5,24] and a recent study of Chauhan *et al.*[25] using a reverse biased dc sputter magnetron source; the former showed the formation of nanoscale striations or ripplelike structures at off-normal angles of beam impingement, and the latter the formation of nanodot patterns at normal incidence of ions extracted from the so-called plasma fireball. The off-normal ion incidence is relatively difficult in plasma, because the ions are usually incident normally onto substrate surfaces after being accelerated through the sheath thereon.[26]

We have investigated surface roughening and rippling during Si etching in Cl-based plasmas, by developing a MC-based three-dimensional atomic-scale cellular model (ASCeM-3D) for plasma-surface interactions and feature profile evolution during plasma etching.[7,27,28] Simulations showed random roughness at normal incidence ($\theta_i = 0°$, relative to the substrate surface normal), while sawtooth-like ripples with their wave vector oriented parallel (crests/troughs elongated perpendicular) to the direction of ion incidence at intermediate off-normal angles ($15° < \theta_i < 60°$), and striations or ripplelike structures with the wave vector perpendicular (crests/troughs parallel) to it at high off-normal angles ($70° < \theta_i < 85°$). We have also conducted experiments on roughening and smoothing (or non-roughening) of initially rough as well as planar surfaces during plasma etching of Si in Cl_2, by varying the ion incident energy ($E_i \approx 20$–500 eV at $\theta_i = 0°$),[7,29,30] to validate the model developed. A comparison of experiments and ACSeM-3D simulations with the help of classical molecular dynamics simulations[31] revealed a crucial role of ion scattering or reflection from feature surfaces on incidence in the formation and evolution of surface roughness (and ripples) during plasma etching.[7,29,30,32]

In this paper, we report on the spontaneous or self-organized formation of nanoscale ripple structures on blank substrate surfaces during plasma etching of Si in Cl_2, using sheath control plates to achieve the off-normal ion incidence thereon. The ion incidence angles onto substrates, set on sidewalls and/or at the bottom of inclined trenches of the plate, were evaluated based on 2D electrostatic particle-in-cell (PIC) simulations of the plasma sheath concerned. Experiments showed surface roughening and rippling in response to ion incidence angle; in particular, they showed clearly well-defined periodic sawtooth-like ripples at intermediate off-normal angles ($\theta_i \approx 40°$), as predicted by ASCeM-3D. This is the first experimental demonstration of the formation of sawtooth-like nanoripples by plasma etching, and also probably one of the most clear demonstrations of it caused by ion bombardment on solid material surfaces (in the fields of ion beam- and plasma-surface interactions), to the best of our knowledge. Plasma etching under off-normal ion incidence has so far been reported using plasma beam,[22,23] Faraday cage,[33–38] and sheath control plate;[39] however, most of them were concerned with the angled etching of lithographically pattered substrates to fabricate 3D device structures.[33–39]

It is noted that nanoripple patterns formed by IBS have today found a variety of applications as rippled substrates/templates for: protein adsorption in biomedical science,[40] fabrication of longitudinal recording media[41] and evolution of a large induced magnetic anisotropy of ferromagnetic films[42,43] in information technology, and formation of ordered arrays of quantum dots,[44] nanoparticles,[45–48] and nanowires[46,49,50] in sensing, photovoltaic, optoelectronic, and/or plasmonic applications. In addition,

the formation of periodic nanoripples by inclined deposition of IBS-sputtered particles has recently been investigated for fabricating a multilayered blazed grating in extreme uv and soft-x ray applications,[51] where a triangular, sawtooth-shaped cross section would be indispensable.

II. EXPERIMENT

Figure 1 shows a schematic of the experimental setup, along with the coordinate system (X, Y, Z) for the plasma/sheath analysis. Experiments employed an inductively coupled plasma (ICP) reactor made of stainless steel as detailed previously:[29] the ICP discharge was established by 13.56-MHz rf powers of P_{ICP} = 450 W in Cl_2 at a flow rate F_0 = 20 sccm and pressure P_0 = 20 mTorr, where a 4-in.-diam wafer stage was rf-biased at 13.56 MHz with being temperature controlled at T_s = 20°C. The rf bias power was fixed at P_{rf} = 150 W to give the ion energy $E_i = V_p - V_{\mathrm{dc}} \approx 470$ eV unless otherwise stated, where V_p and V_{dc} are the plasma potential and dc self-bias voltage at the wafer stage measured by a Langmuir probe (LP) and a voltage probe, respectively. Plasma conditions of the discharge were monitored by LP and optical emission spectroscopy (OES).

The sheath control plate was a square metal plate of Cu, 5 cm on each side and h_s = 4 mm high, consisting of thin blades inclined at an angle θ_s = 45° and 90° to the plate plane and separated by slits of different widths in the range w_s = 3–7 mm;[52] in other words, the plate consisted of an array of inclined trenches of width w_s and depth h_s separated by thin blades. In experiments, the sheath control plate was set into place on the wafer with the plate being electrically connected to the rf-powered wafer stage (cathode), and Si sample substrates for etching were pasted in place on sidewalls and/or at the bottom of the trenches (on upward-facing sidewalls for the plate with $\theta_s < 90°$). The top surfaces of the sheath control plate were covered with an Si plate (not shown, consisting of Si wafer pieces), to prevent the sputtering and redeposition of nonvolatile products (metals and/or metal compounds) over sample substrate surfaces during etching; note that Cu is known to be difficult to etch owing to low-volatility reaction products.[53,54] The potential distributions in the plasma/sheath, together with ion trajectories onto substrate surfaces, were calculated by using the 2D electrostatic PIC method,[55,56] to evaluate the ion incidence angle, flux, and energy on the surfaces being etched.

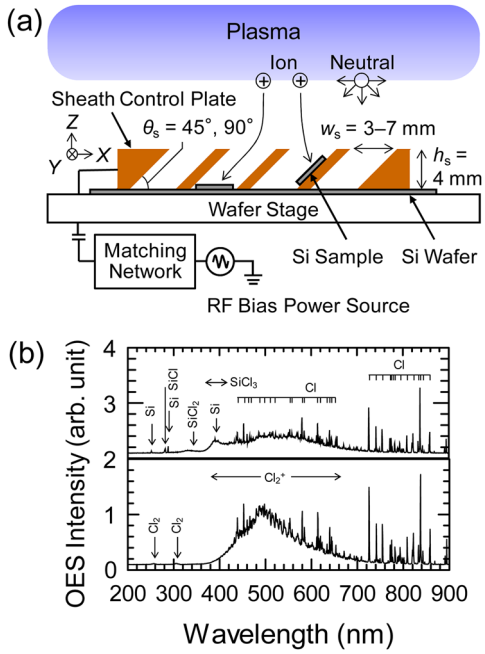

FIG. 1. (a) Schematic of the experimental setup, along with the coordinate system (X, Y, Z) used for the plasma/sheath analysis. Also shown in (b) are typical OES spectra in the wavelength range 200–900 nm during ICP Cl_2 discharge in the presence (upper, P_{rf} = 150 W or $E_i = V_p - V_{\mathrm{dc}} \approx 470$ eV) and absence (lower, P_{rf} = 0 W or $E_i \approx 13$ eV) of Si etching.

Samples for etching were rectangular substrates cut out from a blank Si(100) wafer of *n*-type with a resistivity $\rho_r \approx 10\ \Omega$·cm and thickness of 0.5 mm, which were pre-cleaned through HF acid dipping followed by deionized water rinsing prior to etching. The surface morphology of etched and unetched sample surfaces was examined by atomic force microscopy (AFM) in tapping mode using a silicon cantilever with a nominal tip radius less than 10 nm, to measure the root-mean-square surface roughness (initially, RMS ≈ 0.15 nm) and to analyze the power spectral density (PSD) distribution of surface features. The surface images were also taken by scanning electron microscopy (SEM), and the compositional analysis was performed by energy dispersive x-ray spectroscopy (SEM-EDX). The cross-sectional profile or structure of the surface was characterized by cross-sectional SEM and transmission electron microscopy (TEM), where the specimens were prepared by the standard focused-ion-beam milling technique. The etching time was 2–5 min, and the etched depth was measured by stylus profilometry.

In these experiments, as also shown in Fig. 1, the OES spectra during ICP discharge consisted of atomic lines and molecular bands of Cl_x (x = 1, 2) and Cl_2^+ originating from feed gases in the absence of etching (P_{rf} = 0 W), while additional lines and bands of $SiCl_x$ (x = 0–3) originating from etch products/byproducts were observed to occur in the presence of etching (P_{rf} = 150 W);[29] the latter are more significant at increased P_{rf} (or E_i), corresponding to the increase in etch rate and the resultant increase in concentration of products/byproducts in the plasma, while the former become less significant thereat, corresponding to reduced partial pressures or concentrations of feed gases under operating conditions of constant pressure P_0. Atomic Cu lines (324.7, 327.3, and 333.7 nm)[57] and molecular CuCl bands (435.3, 443.3, and 451.5 nm)[58,59] were not identified, where the former are prominent Cu lines often observed in OES during rf magnetron sputtering of Cu targets,[60] and the latter are CuCl bands observed in OES during pulsed laser ablation of solid CuCl.[61] In addition, metal contaminants (Cu, stainless steel) on etched sample surfaces were found below the present EDX detection sensitivity, although the ion-induced pattern formation on Si caused by metal impurities has been suggested and investigated in IBS studies.[62–65]

Moreover, LP measurements indicated that the plasma ion and electron densities remain almost unchanged at approximately $n_i \approx 3 \times 10^{10}$ cm^{-3} and $n_e \approx 1 \times 10^{10}$ cm^{-3} over the bias power range P_{rf} = 0–150 W investigated, while the electron temperature and plasma potential increase slightly with increasing P_{rf} from $T_e \approx 4.4$ to 5.6 eV and $V_p \approx 15$ to 24 V; the corresponding ion flux concerned (or the ion saturation current to the probe) remains almost constant at approximately $\Gamma_i^0 = 0.61\, n_i (k_B T_e/m_i)^{1/2} \approx (0.5 - 0.6) \times 10^{16}$cm^{-2}s^{-1},[26] where k_B is the Boltzmann constant, m_i is the ion mass, and the probe data were analyzed assuming the mass of predominant ions (e.g., Cl_2^+ at P_{rf} = 0 W and $SiCl^+$ at P_{rf} = 150 W) as detailed previously.[29] The potential difference was measured to increase significantly with increasing P_{rf} from $V_p - V_{dc} \approx 13$ to 470 V, owing to the dc self-bias voltage V_{dc} decreased. Under these conditions, the plasma sheath thickness above a cathode surface (i.e., the distance from the sheath edge to the electrode) was estimated based on the planar sheath theory:[26] $s_0 \approx \varsigma\, \lambda_{D0}$ with the Debye length $\lambda_{D0} = \left(\varepsilon_0 k_B T_e/e^2 n_0\right)^{1/2}$ and a coefficient ζ, where ε_0 is the permittivity of vacuum, e the elementary charge, and n_0 the plasma density; e.g., $\lambda_{D0} \approx 0.090$ and 0.10 mm, ζ = 2.5 and 21, and $s_0 \approx 0.23$ and 2.1 mm at P_{rf} = 0 and 150 W, respectively, assuming $n_0 = n_i$ and $\varsigma \approx \left(2^5 \eta_c^3\right)^{1/4}/3 + (\eta_c/2)^{1/4}$,[66,67] where $\eta_c = e|\phi_c|/k_B T_e$ is the dimensionless cathode potential (referenced to the plasma potential, $|\phi_c| = V_p - V_{dc}$). The dimensions of the sheath control plate (trench width w_s and depth h_s) presently employed were chosen in such a way that sheath overlap occurs above trench features of the cathode (or the sheath edge is pushed out of the trench),[67] as detailed below.

III. RESULTS AND DISCUSSION

A. Sheath control plate

Figure 2 shows the potential distribution and ion trajectories for two different sheath control plates with (θ_s, w_s) = (45°, 5 mm) and (90°, 3 mm), calculated under typical plasma conditions giving an ion incident energy of nominally $E_i \approx$ 100, 200, and 500 eV.[29] Also shown are the corresponding angular distributions of ion fluxes incident on sidewall and bottom surfaces of the trench (for the

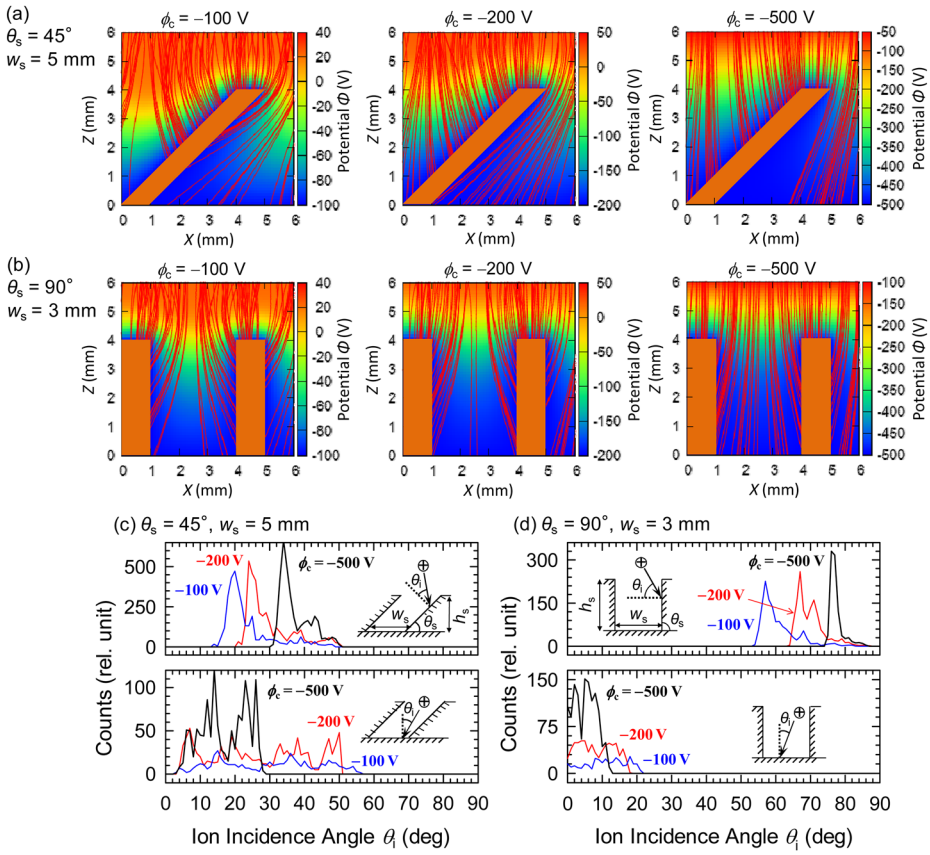

FIG. 2. Potential distribution and ion trajectories in the (X, Z) plane for two different sheath control plates with (θ_s, w_s) = (a) (45°, 5 mm) and (b) (90°, 3 mm), calculated using the 2D electrostatic PIC method (2d/3v) under typical plasma conditions giving an ion incident energy of nominally $E_i \approx 100$, 200, and 500 eV. The calculation domain concerned is $W = 12$ mm in width and $H = 15$ mm high ($0 \le X \le W$, $0 \le Z \le H$). Also shown in (c) and (d) are the corresponding angular distributions of ion fluxes incident on trench sidewall and bottom surfaces of the plates (integrated over the surface). Note that at vertical boundaries, the potential was taken to be $\phi = \phi_0$ at the top (at $Z = H$), and $\phi = \phi_c$ at the sheath control plate (set on the cathode or rf-powered electrode at the bottom $Z = 0$), where $\phi_0 = 30$ V, and $\phi_c = -100$, –200, and –500 V for the case of nominal $E_i = \phi_0 - \phi_c \approx 100$, 200, and 500 eV, respectively.

$\theta_s = 45°$ plate, on the upward-facing sidewall on which substrates for etching are pasted in place). The calculation domain here is a rectangle $W = 12$ mm in width and $H = 15$ mm high ($0 \le X \le W$, $0 \le Z \le H$), and the particles considered are positive Cl_2^+ ions and negative e^- electrons (neglecting Cl^- ions), where background Cl_2 neutrals (or pressures) are not followed assuming simply a collisionless plasma/sheath. The 2D electrostatic PIC code used in this study is based on hybrid electrostatic PIC algorithms,[56] and it is a descendant of fully kinetic PIC codes that we used previously for rf and microwave discharge plasmas (2D electrostatic,[68] 2D electromagnetic,[69,70] 3D electromagnetic[71]). In hybrid PIC, the ions are treated as particles (superparticles), while electrons are assumed to follow the Boltzmann relation $n_e = n_0 \exp[e(\phi - \phi_0)/k_B T_e]$, where ϕ is the electric potential concerned, and n_0 and ϕ_0 are the plasma density and potential at a reference state, respectively; then, the dynamics of ions and the electric field are solved self-consistently with the Poisson equation $\nabla^2\phi = -e(n_i - n_e)/\varepsilon_0$ and the equations of motion for the ions $d(m\mathbf{v})/dt = q\mathbf{E} = -q\nabla\phi$, $\mathbf{v} = d\mathbf{r}/dt$, where q, m, $\mathbf{r}$, and $\mathbf{v}$ denote the charge, mass, position, and velocity of an ion superparticle ($q/m = e/m_i$).

Calculations were made in two space dimensions (X, Z) with three velocity components (2d/3v) and periodic boundary conditions in the horizontal X-direction, according to the general procedure of the PIC simulation method:[55] the velocities and positions of the ion superparticles are updated by integrating explicitly the equations of motion in time, where the velocity Verlet algorithm[72–74] was used as opposed to the leapflog scheme usually applied in many other codes,[55,56,68–71]

since the former tends to converge faster than the latter. The ion densities at the discrete grid points are then calculated by mapping the continuous positions of individual particles (particle weighting). The electric fields at the grid points are then computed by solving implicitly the nonlinear Poisson equation, where a second-order central finite difference approach was used with Broyden's method for iteration (an update of the Newton-Raphson method).[75,76] Then, the electric forces acting on the particles are calculated by interpolating the fields back to the particle positions from the grid points (field weighting). Such a cycle of successive calculations (one time step) is repeated until the potential distribution reaches steady state. The time step was taken to be $\Delta t = 1 \times 10^{-8}$ s, the grid spacing to be $\Delta X = \Delta Z = 0.1$ mm, and the total number of particles in the 2D calculation domain to be $N_p = 9 \times 10^5$ particles [$N_c = (W/\Delta X) \times (H/\Delta Z) = 1.8 \times 10^4$ grid cells, $N_p/N_c = 50$ particles per grid cell], considering plasma conditions ($n_0 = 3 \times 10^{10}$ cm^{-3}, $T_e = 5$ eV) and the constraints imposed in time-explicit hybrid PIC simulation to ensure the accuracy and stability:[55,56] $\Delta t < 0.2/\omega_{pi0}$, $\Delta X/V_{max}$; $\Delta X < \lambda_{D0}$; and $N_p/N_c > 50$. Here, $\omega_{pi0} = \sqrt{e^2 n_0/\varepsilon_0 m_i}$ is the ion plasma frequency ($\omega_{pi0} \approx 2.7 \times 10^7$ rad/s), and $V_{max} \approx \sqrt{2E_i/m}$ is the maximum velocity magnitude of the particles.

At the beginning of calculation, N_p ion superparticles (a weight ~ 20) were loaded uniformly in the domain with a Maxwellian velocity distribution at a temperature of $T_i = 300$ K (0.026 eV). At vertical boundaries of the domain ($0 \le Z \le H$), the potential was taken to be $\phi = \phi_0$ at the top (at $Z = H$), and $\phi = \phi_c$ at the bottom (concretely, on top, sidewall, and bottom surfaces of the trenches of the sheath control plate, set on the cathode or rf-powered electrode at $Z = 0$), where $\phi_0 = 30$ V, and $\phi_c = -100$, –200, and –500 V for the case of nominal $E_i \approx 100$, 200, and 500 eV, respectively. Particles reaching the plate or the lower boundaries were assumed to be lost thereat without any secondary electron emission; these lost particles were re-injected back into the system uniformly at the top of the domain according to a half Maxwellian distribution at T_i, in order to keep the total number N_p of particles in the system relatively constant during calculation. Moreover, after the potential distribution had reached steady state, 6×10^3 sample ions were randomly allocated at the top of the domain, being injected successively thereinto with a vertically downward translational energy of T_i, to calculate single-ion trajectories and then to evaluate the angular distribution of ion fluxes incident on sidewall and bottom surfaces of the trench. Note that in Fig. 2, the angular distributions of ion fluxes represent the relative number of sample ions incident on the respective surfaces of the trench (integrated over the surface) at angles between θ_i and $\theta_i + 1°$ (between $|\theta_i|$ and $|\theta_i| + 1°$ at the rectangular trench bottom for the $\theta_s = 90°$ plate); the sample ion trajectories represent every 50th trajectory calculated (thus, each figure includes ~60 trajectories); in addition, banded trajectories (or locally dense/sparse regions of the trajectories) in the figure are attributed partly to the statistical nature of this procedure for visualization, and partly to some sub-mm-scale microstructures of the sheath that occur in the present PIC simulation (not identified), although the trajectory density is considered to be proportional to the ion flux concerned to some extent.

The results indicate that for both sheath control plates with $\theta_s = 45°$ and 90°, the sheath structure or the potential distribution is distorted by the plate, causing the distortion of ion trajectories to achieve the off-normal incidence on its trench sidewall and bottom surfaces [Figs. 2(a) and 2(b)]. The equipotential surfaces are not planar due to geometrical trench features of the sheath control plate: they are corrugated above the plate (at $Z > h_s = 4$ mm), although the sheath edge [taken to be at $Z = h(X)$ giving $\phi = \phi_0 - k_B T_e/2e \approx 27.5$ V] is pushed out of the trench [$h(X) > h_s$].[67] Here, $k_B T_e/2e \approx 2.5$ V is a potential drop in the presheath,[26] and above the blades, the sheath thickness $s = h - h_s$ is somewhat (about a factor of two) larger than the planar s_0 estimated earlier in Sec. II. Above the blades or above top surfaces of the trench, the equipotental surfaces are concave downward, where the ion trajectories tend to be deflected toward the central part of the blade top surfaces; on the other hand, they are convex downward above and in the trench, where the ion trajectories tend to be deflected toward the trench sidewalls, thus reducing the ion fluxes onto its bottom surfaces.

It is further noted that above and in the rectangular trench of the $\theta_s = 90°$ plate, the potential distribution and ion trajectories are symmetric with respect to the vertical plane at its center [$X = 2.5$ mm, Fig. 2(b)]. On the other hand, they exhibit no symmetry above and in the inclined trench of the $\theta_s = 45°$ plate [Fig. 2(a)]: the equipotential surfaces are convex down toward the downward-facing sidewall of the trench; thus, in the left half space (approximately, $0 \le X < 1$ mm and $5 < X \le 6$ mm), the ion trajectories tend to be deflected to the left, toward the trench downward-facing

sidewall; and those in the right half space (approximately, $1 < X < 4$ mm) tend to be deflected to the right, toward the trench upward-facing sidewall. The geometrical shadowing effects of the inclined blade or trench features for incoming ions tend to be reduced by the potential distortion and thus the ion deflection, giving ion fluxes incident on the downward-facing sidewall of the trench and on its bottom surfaces that are in the shadow of the feature.

As the cathode potential $|\phi_c|$ and thus the ion energy $E_i = \phi_0 - \phi_c$ is increased for both sheath control plates with $\theta_s = 45°$ and 90°, the sheath edge tends to be planar and positioned further away from the plate, and the potential distortion and the ion deflection become less significant; concomitantly, the shadowing effects are enhanced in the inclined trench of the $\theta_s = 45°$ plate. As a result [Figs. 2(c) and 2(d)], on trench sidewalls of both $\theta_s = 45°$ and 90° plates (on the upward-facing sidewall for the former), as $|\phi_c|$ or E_i is increased, the ion incidence angles θ_i tend to increase and to approach the respective blade or trench angles θ_s with their distribution $\Delta\theta_i$ being narrowed. On the other hand, on trench bottom surfaces of both plates, as $|\phi_c|$ or E_i is increased, the ion incidence angles θ_i ($|\theta_i|$ for the $\theta_s = 90°$ plate) tend to decrease and to approach the angle 0° of normal incidence also with their distribution $\Delta\theta_i$ being narrowed. The angular distribution of ion incident fluxes for $\phi_c = -500$ V or $E_i \approx 500$ eV gives an incidence angle of nominally $\theta_i \approx 40°$ and 80° with a full width at half maximum $\Delta\theta_i \approx 10°$ and 2° on trench sidewalls of the $\theta_s = 45°$ and 90° plates, respectively, while $\theta_i \approx 20°$ and 10° with $\Delta\theta_i \approx 15°$ and 10° on its bottom surfaces of the respective plates. Note that on trench sidewall and bottom surfaces of both plates, the incidence angle θ_i varies from position to position on the surface [as seen in Figs. 2(a) and 2(b)], which leads to the distribution $\Delta\theta_i$ of it: θ_i on sidewalls decreases and then increases in the direction toward the bottom, while θ_i or $|\theta_i|$ on bottom surfaces increases in the direction toward sidewalls (toward the downward-facing sidewall for the $\theta_s = 45°$ plate). In addition, the angular distribution of ion fluxes depends also on trench width w_s (not shown): as w_s is increased, the equipotential surfaces are more convex downward above and in the trench, the sheath edge tends to penetrate into the trench, the ion deflection tends to be more significant therein, and so the distribution $\Delta\theta_i$ of ion incidence angles tends to be broadened.

B. Formation of surface ripples

Figure 3 shows representative AFM images (top view, 1×1 μm^2) of Si surfaces etched in Cl_2 plasma with two different nominal $\theta_i \approx 40°$ and 80° (on trench sidewalls) at $E_i = V_p - V_{dc} \approx 470$ eV, using the two sheath control plates as analyzed in Fig. 2. Also shown are the corresponding angle-view images (0.5×0.5 μm^2), along with the coordinate system (x, y, z) for the analysis of surface features, where the x- and y-directions correspond to that parallel and perpendicular to the direction of ion incidence, respectively. The etching time here was 3 min for $\theta_i \approx 40°$ and 5 min for $\theta_i \approx 80°$, giving the respective etch rates ER ≈ 360 and 20 nm/min and rms roughness RMS ≈ 6.3 and 4.9 nm; the respective ion fluxes onto surfaces being etched were estimated to be $\Gamma_i^s \approx \Gamma_i^0 \times \cos\theta_i \approx 0.38$ and 0.087×10^{16} cm^{-2}s^{-1} based on LP measurements, and thus the respective ion fluences (= flux $\Gamma_i^s \times$ time) to be $\Phi \approx 6.8$ and 2.6×10^{17} cm^{-2} thereon. The AFM images exhibit parallel-mode ripples for intermediate $\theta_i \approx 40°$, while relatively weak perpendicular-mode ones for high $\theta_i \approx 80°$, as predicted by ASCeM-3D simulations;[7,27,28] note that Si substrates etched without sheath control plates and also etched on top surfaces of the plates showed smooth surface features with random roughness (no ripplelike structures at normal $\theta_i = 0°$, where ER ≈ 520 nm/min and RMS ≈ 0.4 nm).[29,30] From the line scans across the AFM images, the wavelengths or distances (peak-to-peak/valley-to-valley) of the ripples were evaluated to be in the range $\lambda_r \approx 30$–100 nm for $\theta_i \approx 40°$ and $\lambda_r \approx 50$–150 nm for $\theta_i \approx 80°$, and their amplitudes (peak-to-valley) were in the range $z_r \approx 10$–20 nm for $\theta_i \approx 40°$ and $z_r \approx 2$–10 nm for $\theta_i \approx 80°$. The PSD analysis of AFM images gave similar ripple sizes: a pronounced peak of the 1D-PSD distribution $P_x(k_x)$ at a spatial frequency $k_x \approx 0.015$ nm^{-1} for $\theta_i \approx 40°$ corresponds to the mean $\lambda_r \approx 65$ nm, while a less pronounced peak of $P_y(k_y)$ at $k_y \approx 0.01$ nm^{-1} for $\theta_i \approx 80°$ to the mean $\lambda_r \approx 100$ nm.

Figure 4 shows representative cross-sectional TEM images (with low and high magnifications) of Si surfaces etched as in Fig. 3, where the specimens are those cut parallel and perpendicular to the direction of ion incidence for $\theta_i \approx 40°$ and 80°, respectively. The TEM images for $\theta_i \approx 40°$ clearly exhibit well-defined periodic sawtooth-like ripples, where their average wavelength and amplitude

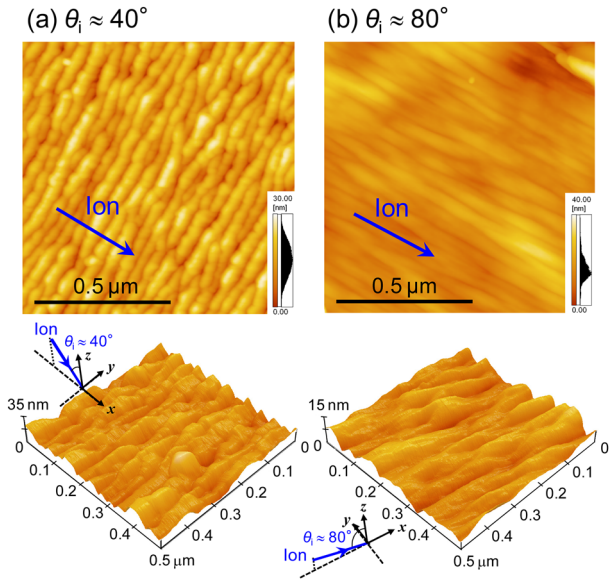

FIG. 3. AFM images (top view, $1 \times 1\ \mu m^2$) of Si surfaces etched in Cl_2 plasma with two different nominal ion incidence angles of $\theta_i \approx$ (a) 40° and (b) 80° on substrate surfaces at $E_i = V_p - V_{dc} \approx 470$ eV, using the two sheath control plates as analyzed in Fig. 2. Also shown are the corresponding angle-view images ($0.5 \times 0.5\ \mu m^2$), along with the coordinate system (x, y, z) used for the analysis of surface features. Sample substrates for etching were pasted in place on trench sidewalls of the plates, and the etching time was 3 min for $\theta_i \approx 40°$ and 5 min for $\theta_i \approx 80°$.

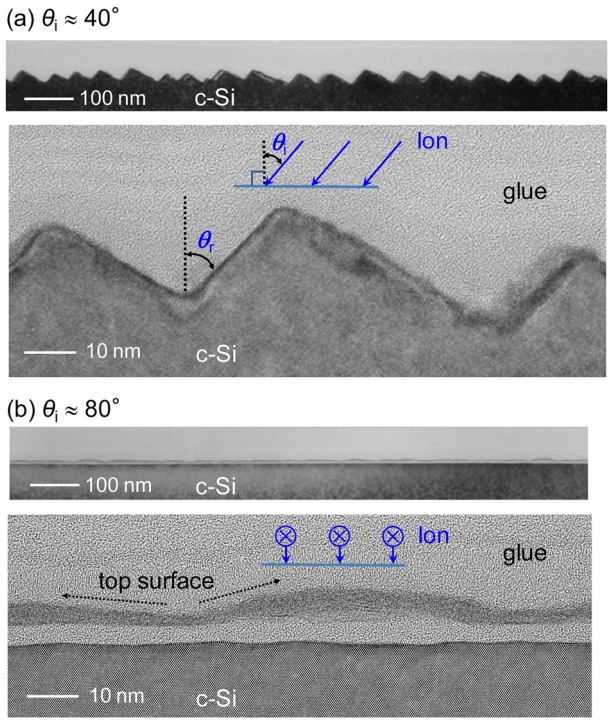

FIG. 4. Cross-sectional TEM images (with low and high magnifications) of Si surfaces etched in Cl_2 plasma with two different $\theta_i \approx$ (a) 40° and (b) 80° at $E_i \approx 470$ eV as in Fig. 3, where the specimens (~100 nm in thickness) are those cut out parallel and perpendicular to the direction of ion incidence, respectively. In (a), the ripple angle θ_r is defined as the angle between the downward slope of the ripple and the surface normal of substrates.

are evaluated to be approximately $\lambda_r \approx 62$ nm and $z_r \approx 18$ nm from the low magnification image, being consistent with those from the AFM images as mentioned above. The high magnification image indicates that the ripple angle θ_r between the downward slope of the ripple and the surface normal of substrates is correlated with the ion incidence angle as $\theta_r \approx \theta_i$: the ripple downward-sloping surfaces are nearly parallel to the ion incidence, while the upward-sloping ones are nearly perpendicular to it. This characteristic profile is assumed to reflect the formation of ripple structures under shadowing effects of the feature for incoming ions and those of faceting caused by the surface curvature-dependent etch yields (or the yields depending on the local ion incidence angle θ relative to the local feature-surface normal, generally $\theta \neq \theta_i$).[77,78] The limiting condition for shadowing not to occur and faceting to be fully developed, $\tan(\pi/2 - \theta_i) \geq 2\pi h_0/\lambda_r$,[78] gets satisfied here: $\tan(\pi/2 - \theta_i) \approx 1.2$, while $2\pi h_0/\lambda_r \approx 0.91$ with $h_0 = z_r/2$.

Sawtooth-like (or terrace-like) ripples have been observed for parallel-mode ripples in IBS experiments through cross-sectional TEM,[79–81] SEM,[82] and AFM line scan;[83–89] typically, λ_r (nm)/z_r (nm) $\approx$ 500/40 for 20-keV Ga^+ on diamond at $\theta_i = 80°$,[79,80] $\approx$ 250/50 for 12-keV N^+ on Si at 60°,[81] $\approx$ 400/150 for 30-keV Ga^+ on $Cd_2Nb_2O_7$ at 45°,[82] $\approx$ 3000/500 for 60-keV Ar^+ on Si at 60°,[83] $\approx$ 2000/450 for 16.7-keV O_2^+ on Al at 45°,[84] $\approx$ 550/10 for 0.5-keV Ar^+ on mica at 60°,[85] $\approx$ 350/55 for 0.5-keV Ar^+ on Si at 70°,[86,87] $\approx$ 60/5 for 1.2-keV Xe^+ on Si at 75°,[88] and $\approx$ 40/5 for 2-keV Kr^+ on Si at 75°.[89] Among these, the first three[79–82] and the last three[86–89] showed fully developed sawtooth-like profiles with $\theta_r \approx \theta_i$ similar to the present experiments.

On the other hand, the TEM images for $\theta_i \approx 80°$ exhibit weakly corrugated surfaces, consisting of upper (darkened) and lower amorphous layers (< 10 nm thick in total) on crystalline Si (c-Si) substrates, where the corrugation is significantly weak on c-Si surfaces at the bottom as compared with that on top surfaces. The wavelengths and amplitudes of corrugations or ripplelike structures estimated from the TEM images are on the order of $\lambda_r \approx 100$ nm and $z_r \approx 5$ nm at the top of amorphous layers, which would be reflected on the corresponding AFM images [Fig. 3(b)]. The amorphous layers observed may be related to the ion scattering-caused surface channeling effects at high off-normal incidence,[90] although no cross-sectional images to be compared have been reported for perpendicular-mode ripples in IBS.

Figure 5 shows the wavelengths λ_r and amplitudes z_r of sawtooth-like ripples with $\theta_r \approx \theta_i$ for intermediate $\theta_i = 40°–60°$, observed in the present experiments, IBS experiments,[81,82]

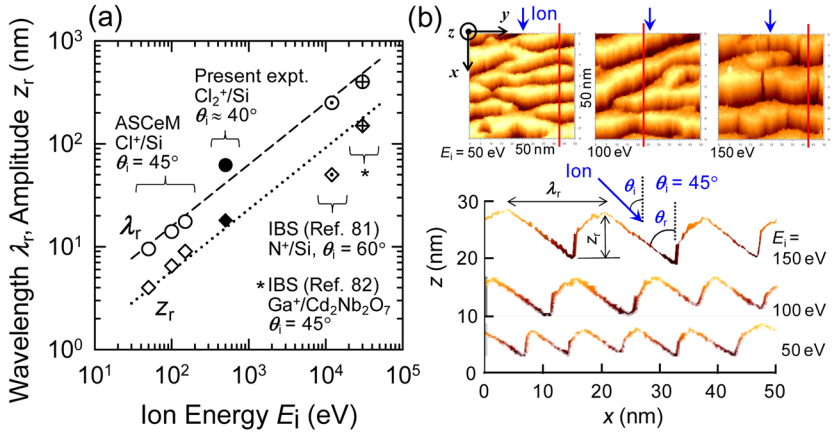

FIG. 5. (a) Wavelengths λ_r (peak-to-peak/valley-to-valley) and amplitudes z_r (peak-to-valley) of fully developed sawtooth-like ripples with the ripple angle $\theta_r \approx \theta_i$ for intermediate $\theta_i = 40°–60°$, observed in the present experiments, IBS experiments,[81,82] and ASCeM-3D simulations[7,27,28,32] at different $E_i = 0.05–30$ keV. The broken and dotted lines are for guiding the eyes, representing the scaling $\lambda_r \sim E_i^p$ and $z_r \sim E_i^q$ with $p, q \approx 0.6$. Also shown for reference are (b) typical ASCeM-3D-simulated surface features of Si (top view, 50 × 50 nm^2) at $t = 60$ s after the start of etching in Cl_2 plasma for $\theta_i = 45°$ at $E_i = 50$, 100, and 150 eV, together with the corresponding side or cross-sectional views of surface features (the data have been vertically shifted for the sake of clarity). The line of sight is perpendicular to the direction of ion incidence (or in the y-direction), and the simulation domain shown is 2 nm in width (in the y-direction at around the x-axis indicated by the vertical red lines in the respective top views).

and ASCeM-3D simulations[7,27,28,32] at different $E_i = 0.05 - 30$ keV, indicating the scaling $\lambda_r \sim E_i^p$ and $z_r \sim E_i^q$ with $p, q \approx 0.6$. Also shown for reference are the typical ASCeM-3D-simulated surface features of Si (top view, 50×50 nm^2) at $t = 60$ s after the start of etching in Cl_2 plasma for $\theta_i = 45°$ at $E_i = 50$, 100, and 150 eV, together with the corresponding side or cross-sectional views. The ASCeM-3D takes into account a variety of surface chemistry and kinetics concerned with plasma etching,[7,27,28] including the ion scattering or reflection from feature surfaces on incidence into vacuum and/or its penetration into substrates, surface reemission of neutrals, and geometrical shadowing of the feature. Simulations were made for square substrates 50 nm on a side with initially flat surfaces (RMS = 0) assuming similar conditions to experiments:[29,30] an incoming ion (Cl^+) flux ${\Gamma_i}^0 = 1.0 \times 10^{16}$ cm^{-2}s^{-1} (fluence $\Phi = 4.2 \times 10^{17}$ cm^{-2}), ion temperature $k_B T_i = 0.5$ eV, neutral reactant (Cl)-to-ion flux ratio ${\Gamma_n}^0/{\Gamma_i}^0 = 100$, and neutral temperature $T_g = 500$ K, in the absence of incoming inhibitors such as oxygen and byproducts (${\Gamma_o}^0 = {\Gamma_p}^0 = 0$); the sticking probability $S_q = 0.05$ was assumed for redeposition of etch/sputter products, along with the dopant concentration $N_e = 1.0 \times 10^{18}$ cm^{-3} and surface temperature $T_s = 320$ K of substrates. These ASCeM-3D simulations gave the respective etch rates ER ≈ 140, 260, and 340 nm/min, rms surface roughness RMS ≈ 1.7, 2.1, and 2.4 nm, and ripple traveling velocities $v_r \approx 3.4$, 5.5, and 7.2 nm/s laterally in the direction of ion incidence[7,32] (a little higher than the vertically downward v_{ER} = ER/60 ≈ 2.3, 4.3, and 5.7 nm/s) at $t = 60$ s or at steady state.

The ripple wavelength and amplitude in IBS are appreciated to rely on ion energy, incidence angle, and fluence (or sputtering time).[18–21] The scaling presently identified in Fig. 5 suggests that the self-organized formation of nanoscale ripple structures through ion bombardment is largely affected not only by the ion shadowing and faceting[77,78] but also by the ion reflection and re-impingement on feature surfaces;[91] in practice, ASCeM-3D simulations without taking into account the effects of ion reflection show no ripple structures but smooth surfaces.[32] Further investigations are needed to unravel all the mechanisms and to control the ripple formation during plasma etching, including the experiments for different E_i, θ_i, and etching times and the model improvements; in practice, the present ASCeM-3D (validated for $\theta_i = 0°$ at $E_i = 20$–500 eV[7,28–30]) reproduces the formation of sawtooth-like ripples at $E_i < 200$ eV, while it exhibits scale-like (or roof tile-like) ripple structures at higher $E_i > 200$ eV;[7,28] this may be partly due to the simulation domain size, which might limit the evolution of longer-wavelength ripple structures perpendicular as well as parallel to the direction of ion incidence.

IV. CONCLUSIONS

We have demonstrated the nanoripple formation in response to ion incidence angle during ICP plasma etching of Si in Cl_2 ($E_i \approx 500$ eV) using sheath control plates to achieve the off-normal ion incidence on substrate surfaces. The ion incidence angles onto substrates, set on sidewalls and/or at the bottom of inclined trenches of the plate, were evaluated based on 2D electrostatic PIC simulations of the plasma sheath concerned. Experiments showed parallel-mode, well-defined periodic sawtooth-like ripples at intermediate off-normal angles ($\lambda_r \sim 60$ nm, $\theta_i \approx 40°$), while perpendicular-mode ripples having weak corrugations or ripplelike structures at high off-normal angles ($\lambda_r \sim 100$ nm, $\theta_i \approx 80°$). The MC-based ASCeM-3D simulations predicted well these observations, suggesting the mechanisms responsible for the ripple formation through ion bombardment during plasma etching (and IBS). The results would be intriguing and informative for ion beam-as well as plasma-surface interactions, since a number of IBS studies have so far been concerned with the ion-induced ripple formation,[16–21] including that of sawtooth-like ripples[79–89] and the mechanisms responsible for it.[92–94] Plasma etching may be promising for the self-organized formation of ordered surface nanostructures such as sawtooth-like ripples as an alternative to IBS.

ACKNOWLEDGMENTS

This work was supported by Grants-in-Aid for Scientific Research (21110008 and 15H03582) from MEXT and JSPS, Japan. One of the authors (K.O.) gratefully thanks Prof. Y. Setsuhara (Osaka University) for kind support throughout preparing this article.

[1] C. G. N. Lee, K. J. Kanarik, and R. A. Gottscho, J. Phys. D: Appl. Phys. **47**, 273001 (2014).
[2] K. J. Kanarik, T. Lill, E. A. Hudson, S. Sriraman, S. Tan, J. Marks, V. Vahedi, and R. A. Gottscho, J. Vac. Sci. Technol. A **33**, 020802 (2015).
[3] K. Patel, T.-J. King Liu, and C. J. Spanos, IEEE Trans. Electron Devices **56**, 3055 (2009).
[4] X. Sun and T.-J. King Liu, IEEE Trans. Semicond. Manuf. **23**, 311 (2010).
[5] W. Guo and H. H. Sawin, J. Phys. D: Appl. Phys. **42**, 194014 (2009), and references therein.
[6] G. S. Oehrlein, R. J. Phaneuf, and D. B. Graves, J. Vac. Sci. Technol. A **29**, 010801 (2011), and references therein.
[7] K. Ono, N. Nakazaki, H. Tsuda, Y. Takao, and K. Eriguchi, J. Phys. D: Appl. Phys. **50**, 414001 (2017), and references therein.
[8] D. L. Goldfarb, A. P. Mahorowala, G. M. Gallatin, K. E. Petrillo, K. Temple, M. Angelopoulos, S. Rasgon, H. H. Sawin, S. D. Allen, M. C. Lawason, and R. W. Kwong, J. Vac. Sci. Technol. B **22**, 647 (2004).
[9] E. Gogolides, V. Constantoudis, G. P. Patsis, and A. Tserepi, Microelectron. Eng. **83**, 1067 (2006).
[10] G. Kokkoris, V. Constantoudis, and E. Gogolides, IEEE Trans. Plasma Sci. **37**, 1705 (2009).
[11] R. L. Bruce, F. Weilnboeck, T. Lin, R. J. Phaneuf, G. S. Oehrlein, B. K. Long, C. G. Wilson, and A. Alizadeh, J. Vac. Sci. Technol. B **29**, 041604 (2011).
[12] L. Azarnouche, E. Pargon, K. Menguelti, M. Fouchier, O. Joubert, P. Gouraud, and C. Verove, J. Vac. Sci. Technol. B **31**, 012205 (2013).
[13] E. Gogolides, V. Constantoudis, G. Kokkoris, D. Kontziampasis, K. Tsougeni, G. Boulousis, M. Vlachopoulou, and A. Tserepi, J. Phys. D: Appl. Phys. **44**, 174021 (2011).
[14] G. Kokkoris and E. Gogolides, J. Phys. D: Appl. Phys. **45**, 165204 (2012).
[15] J. Bae and I. J. Lee, Sci. Rep. **5**, 10126 (2015).
[16] G. Carter, J. Phys. D: Appl. Phys. **34**, R1 (2001), and references therein.
[17] M. A. Makeev, R. Cuerno, and A.-L. Barabási, Nucl. Instrum. Methods B **197**, 185 (2002), and references therein.
[18] W. L. Chan and E. Chason, J. Appl. Phys. **101**, 121301 (2007), and references therein.
[19] T. K. Chini, D. P. Datta, and S. R. Bhattacharyya, J. Phys.: Condens. Matter **21**, 224004 (2009), and references therein.
[20] A. Keller and S. Facsko, Materials **3**, 4811 (2010), and references therein.
[21] J. Munõz-Garcí, L. Vázquez, M. Castro, R. Gago, A. Redondo-Cubero, A. Moreno-Barrado, and R. Cuerno, Mater. Sci. Eng. R **86**, 1 (2014), and references therein.
[22] Y. Yin, S. Rasgon, and H. H. Sawin, J. Vac. Sci. Technol. B **24**, 2360 (2006).
[23] Y. Yin and H. H. Sawin, J. Vac. Sci. Technol. A **25**, 802 (2007); **26**, 151 (2008).
[24] W. Guo and H. H. Sawin, J. Vac. Sci. Technol. A **28**, 259 (2010).
[25] S. Chauhan, T. Barman, M. Bhatnagar, M. Ranjan, and S. Mukherjee, Rev. Sci. Instrum. **88**, 063507 (2017).
[26] M. A. Lieberman and A. J. Lichtenberg, *Principles of Plasma Discharges and Materials Processing*, 2nd ed. (Wiley, Hoboken, NJ, 2005).
[27] H. Tsuda, Y. Takao, K. Eriguchi, and K. Ono, Jpn. J. Appl. Phys. **51**, 08HC01 (2012).
[28] H. Tsuda, N. Nakazaki, Y. Takao, K. Eriguchi, and K. Ono, J. Vac. Sci. Technol. B **32**, 031212 (2014).
[29] N. Nakazaki, H. Tsuda, Y. Takao, K. Eriguchi, and K. Ono, J. Appl. Phys. **116**, 223302 (2014).
[30] N. Nakazaki, H. Matsumoto, H. Tsuda, Y. Takao, K. Eriguchi, and K. Ono, Appl. Phys. Lett. **109**, 204101 (2016).
[31] N. Nakazaki, Y. Takao, K. Eriguchi, and K. Ono, Jpn. J. Appl. Phys. **53**, 056201 (2014); J. Appl. Phys. **118**, 233304 (2015); Jpn. J. Appl. Phys. (in preparation).
[32] T. Hatsuse, N. Nakazaki, H. Tsuda, Y. Takao, K. Eriguchi, and K. Ono (submitted).
[33] G. D. Boyd, L. A. Coldren, and F. G. Storz, Appl. Phys. Lett. **36**, 583 (1980).
[34] B.-O. Cho, S.-W. Hwang, J.-H. Ryu, H.-W. Kim, and S. H. Moon, Electrochem. Solid State Lett. **2**, 129 (1999).
[35] J.-K. Lee, S.-H. Lee, J.-H. Min, I.-Y. Jang, C.-K. Kim, and S. H. Moon, J. Electrochem. Soc. **156**, D222 (2009).
[36] M. J. Burek, N. P. de Leon, B. J. Shields, B. J. M. Hausmann, Y. Chu, Q. Quan, A. S. Zibrov, H. Park, M. D. Lukin, and M. Lončar, Nano Lett. **12**, 6084 (2012).
[37] P. Latawiec, M. J. Burek, Y.-I. Sohn, and M. Lončar, J. Vac. Sci. Technol. B **34**, 041801 (2016).
[38] D. B. Burckel, P. S. Finnegan, M. D. Henry, P. J. Resnick, R. L. Jarecki, Jr., and App. Phys. Lett. **108**, 142103 (2016).
[39] S. Takahashi, K. Suzuki, M. Okano, M. Imada, T. Nakamori, Y. Ota, K. Ishizaki, and S. Noda, Nat. Mater. **8**, 721 (2009).
[40] J. Sommerfeld, J. Richter, R. Niepelt, S. Kosan, T. F. Keller, K. D. Jandt, and C. Ronning, Biointerphases **7**, 55 (2012).
[41] K. Sato, I. Okamoto, Y. Kitamoto, and S. Ishida, Jpn. J. Appl. Phys. **46**, 5139 (2007).
[42] R. Moroni, D. Sekiba, F. B. de Mongeot, G. Gonella, C. Boragno, L. Mattera, and U. Valbusa, Phys. Rev. Lett. **91**, 167207 (2003).
[43] J. Fassbender, T. Strache, M. O. Liedke, D. Markó, S. Wintz, K. Lenz, A. Keller, S. Facsko, I. Mönch, and J. McCord, New J. Phys. **11**, 125002 (2009).
[44] L.-C. Chao, W.-R. Chen, J.-W. Chen, S.-M. Lai, and G. Keiser, J. Vac. Sci. Technol. B **29**, 051805 (2011).
[45] S. Camelio, D. Babonneau, D. Lantiat, and L. Simonot, EPL (Europhys. Lett.) **79**, 47002 (2007).
[46] M. Ranjan and S. Facsko, Nanotechnology **23**, 485307 (2012).
[47] M. Ranjan, S. Facsko, M. Fritzsche, and S. Mukherjee, Microelectron. Eng. **102**, 44 (2013).
[48] M. Ranjan, M. Bhatnagar, and S. Mukherjee, J. Appl. Phys. **117**, 103106 (2015).
[49] M. Ranjan, T. W. H. Oates, S. Facsko, and W. Möller, Opt. Lett. **35**, 2576 (2010).
[50] A. Belardini, M. C. Larciprete, M. Centini, E. Fazio, C. Sibilia, M. Bertolotti, A. Toma, D. Chiappe, and F. B. de Mongeot, Opt. Express **17**, 3603 (2009).
[51] D. L. Voronov, P. Gawlitza, S. Braun, and H. A. Padmore, J. Appl. Phys. **122**, 115303 (2017).
[52] N. Nakazaki, H. Matsumoto, S. Sonobe, H. Tsuda, Y. Takao, K. Eriguchi, and K. Ono, in *Proc. 37th Int. Symp. on Dry Process*, DPS2015 (JSAP, Tokyo, 2015), pp. 13–14.
[53] J. W. Lee, Y. D. Park, J. R. Childress, S. J. Pearton, F. Sharifi, and F. Ren, J. Electrochem. Soc. **145**, 2585 (1998).
[54] S. Lee and Y. Kuo, J. Electrochem. Soc. **148**, G524 (2001).

[55] C. K. Birdsall and A. B. Langdon, *Plasma Physics via Computer Simulation* (McGraw-Hill, New York, 1984).
[56] K. L. Cartwright, J. P. Verboncoeur, and C. K. Birdsall, Phys. Plasmas **7**, 3252 (2000).
[57] A. R. Striganov and N. S. Sventitskii, *Tables of Spectral Lines of Neutral and Ionized Atoms* (IFI/Plenum, New York, 1968).
[58] R. W. B. Pearse and A. G. Gaydon, *The Identification of Molecular Spectra*, 3rd ed. (Chapman & Hall, London, 1963).
[59] K. P. Huber and G. Hertzberg, *Molecular Spectra and Molecular Structure: IV. Constants of Diatomic Molecules* (Van Nostrand Reinhold, New York, 1979).
[60] J. Posada, A. Bousquet, M. Jubault, D. Lincot, and E. Tomasella, Plasma Process. Polym. **13**, 997 (2016).
[61] J. E. Rothenberg, G. Koren, and J. J. Ritsuko, J. Appl. Phys. **57**, 5072 (1985).
[62] S. Macko, F. Frost, B. Ziberi, D. F. Förster, and T. Michely, Nanotechnology **21**, 085301 (2010).
[63] J. Zhou, S. Facsko, M. Lu, and W. Möller, J. Appl. Phys. **109**, 104315 (2011).
[64] K. Zhang, M. Brötzmann, and H. Hofsäss, AIP Adv. **2**, 032123 (2012).
[65] S. K. Vayalil, A. Gupta, S. V. Roth, and V. Ganesan, J. Appl. Phys. **117**, 024309 (2015).
[66] T. E. Sheridan, J. Phys. D: Appl. Phys. **42**, 015212 (2009).
[67] T. E. Sheridan and T. E. Steinberger, J. Appl. Phys. **121**, 233301 (2017).
[68] Y. Takao, K. Matsuoka, K. Eriguchi, and K. Ono, Jpn. J. Appl. Phys. **50**, 08JC02 (2011).
[69] Y. Takao, N. Kusaba, K. Eriguchi, and K. Ono, J. Appl. Phys. **108**, 093309 (2010).
[70] Y. Takao, K. Eriguchi, and K. Ono, J. Appl. Phys. **112**, 093306 (2012).
[71] Y. Takao, H. Koizumi, K. Komurasaki, K. Eriguchi, and K. Ono, Plasma Sources Sci. Technol. **23**, 064004 (2014).
[72] E. Erden and I. Rafatov, Contrib. Plasma Phys. **54**, 626 (2014).
[73] A. Sun, M. M. Becker, and D. Loffhagen, Compt. Phys. Commun. **206**, 35 (2016).
[74] M. M. Becker, H. Kählert, A. Sun, M. Bonitz, and D. Loffhagen, Plasma Sources Sci. Technol. **26**, 044001 (2017).
[75] J. E. Dennis, Jr. and J. J. Moré, SIAM Rev. **19**, 46 (1977).
[76] G. P. Strivastava, J. Phys. A: Math. Gen. **17**, L317 (1984).
[77] R. M. Bradley and J. M. E. Harper, J. Vac. Sci. Technol. A **6**, 2390 (1988).
[78] G. Carter, J. Appl. Phys. **85**, 455 (1999).
[79] D. P. Adams, M. J. Vasile, T. M. Mayer, and V. C. Hodges, J. Vac. Sci. Technol. B **21**, 2334 (2003).
[80] D. P. Adams, T. M. Mayer, M. J. Vasile, and K. Archuleta, Appl. Surf. Sci. **252**, 2432 (2006).
[81] P. Karmakar and B. Satpati, J. Appl. Phys. **120**, 025310 (2016).
[82] Q. Wei, J. Lian, L. A. Boatner, L. M. Wang, and R. C. Ewing, Phys. Rev. B **80**, 085413 (2009).
[83] D. P. Datta and T. K. Chini, Phys. Rev. B **69**, 235313 (2004).
[84] P. Mishra and D. Ghose, J. Appl. Phys. **105**, 014304 (2009).
[85] A. Metya, D. Ghose, S. A. Mollick, and A. Majumdar, J. Appl. Phys. **111**, 074306 (2012).
[86] T. Basu, J. R. Mohanty, and T. Som, Appl. Surf. Sci. **258**, 9944 (2012).
[87] T. Basu, D. P. Datta, and T. Som, Nanoscale Res. Lett. **8**, 289 (2013).
[88] M. Teichmann, J. Lorbeer, F. Frost, and B. Rauschenbach, Nanoscale Res. Lett. **9**, 439 (2014).
[89] M. Engler, S. Macko, F. Frost, and T. Michely, Phys. Rev. B **89**, 245412 (2014).
[90] Y. Rosandi and H. M. Urbassek, Phys. Rev. B **85**, 155430 (2012).
[91] W. Hauffe, Phys. Status Solidi A **35**, K93 (1976).
[92] E. Chason and W. L. Chan, J. Phys.: Condens. Matter **21**, 224016 (2009).
[93] D. A. Pearson and R. M. Bradley, J. Phys.: Condens. Matter **27**, 015010 (2015).
[94] M. P. Harrison and R. M. Bradley, J. Appl. Phys. **121**, 054308 (2017); **121**, 225304 (2017).